

Article

Automatic Detection of Electric Field VLF Electromagnetic Wave Abnormal Disturbance on Zhangheng-1 Satellite

Ying Han ¹, Jing Yuan ¹, Jianping Huang ^{2,*}, Zhong Li ¹  and Xuhui Shen ²

¹ School of Information Engineering, Institute of Disaster Prevention, Langfang 065201, China; hanying@cidp.edu.cn (Y.H.); yuanjing@cidp.edu.cn (J.Y.); lizhong@cidp.edu.cn (Z.L.)

² National Institute of Natural Hazards, Ministry of Emergency Management of China, Beijing 100085, China; xuhuishen@ninhm.ac.cn

* Correspondence: jianpinghuang@ninhm.ac.cn

Abstract: Ionosphere disturbances are mainly caused by solar activities and earth surface activities. Different electromagnetic wave disturbances show different shapes on the spectrogram, such as artificial very low frequency transmitting stations, power systems, and satellite platform disturbances which all show a horizontal shape. Due to the electric field coupling or superposition by other electromagnetic disturbances, the horizontal electromagnetic wave clarity on the spectrogram is reduced, interrupted, or disappears. Aiming at this phenomenon, based on computer vision technology, this paper proposes an automatic detection and recognition algorithm for the space electric field abnormal interference. Firstly, the horizontal electromagnetic wave on the spectrogram is detected, and then the detected window density on the horizontal line is counted. We then record and save the density anomaly windows on multiple horizontal lines at the same time, so as to realize the electric field anomaly disturbance automatic detection. The accuracy of the algorithm for detecting continuous electromagnetic wave disturbance with a wide frequency and time interval is up to 98.2%. Through the space electromagnetic disturbances automatic identification from massive data, combined with space events and multi-dimensional information, such as time, space and orbit, it is helpful to further find out the global space-time transformation laws of space events.

Keywords: Zhangheng-1 satellite; horizontal straight line detection; computer vision; electromagnetic disturbance detection



Citation: Han, Y.; Yuan, J.; Huang, J.; Li, Z.; Shen, X. Automatic Detection of Electric Field VLF Electromagnetic Wave Abnormal Disturbance on Zhangheng-1 Satellite. *Atmosphere* **2022**, *13*, 807. <https://doi.org/10.3390/atmos13050807>

Academic Editor: Yuichi Otsuka

Received: 26 April 2022

Accepted: 12 May 2022

Published: 15 May 2022

Publisher's Note: MDPI stays neutral with regard to jurisdictional claims in published maps and institutional affiliations.



Copyright: © 2022 by the authors. Licensee MDPI, Basel, Switzerland. This article is an open access article distributed under the terms and conditions of the Creative Commons Attribution (CC BY) license (<https://creativecommons.org/licenses/by/4.0/>).

1. Introduction

The use of electromagnetic satellites to monitor earthquakes began in the 1980s, and a large amount of electromagnetic anomaly information has been detected [1–7], including solar magnetic storms, substorms, lightning, atmosphere, tides, artificial Very low frequency (VLF) transmission stations, power systems, satellite platforms, etc. Different space events show different shapes on the spectrogram [8]. For example, artificial VLF transmitting stations, power systems, and satellite platform disturbances all show a horizontal shape.

The artificial VLF transmitting station emits continuous electromagnetic waves at a fixed frequency between 10 kHz and 50 kHz. Due to the constant frequency, it presents as a quasi-horizontal shape on the spectrogram [9]. When ionospheric disturbances caused by earthquakes occur, ionospheric ion composition and density change, which can be clearly identified in electromagnetic field frequency images under normal circumstances [10]. When the seismic disturbance is generated, Feiyu He et al. [11] found that the propagation of VLF artificial source electromagnetic signals in the ionosphere is stifled, which shows the electric field spectrum value weakening, as shown in Figure 1. Xuemin Zhang et al. [12] believe that it is possible that a large-scale disturbed electric field is generated during earthquake preparation and superimposed on the original background field. The newly added background electric field strengthens the change of the original electric field, or the

background field may be partially or completely covered up, which will lead to the VLF artificial source signal weakening or disappearing.

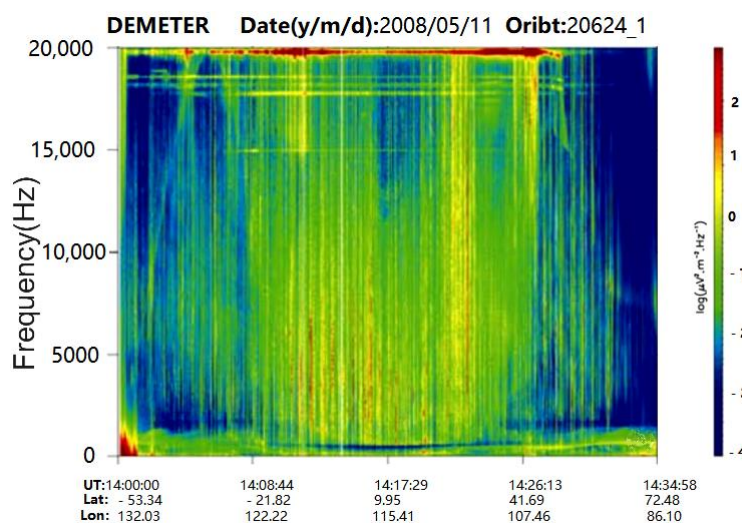


Figure 1. The spectrogram of the electric field component of the VLF electromagnetic signal received by the EFD of the DEMETER satellite passing by the epicenter on 11 May 2018.

Power Line Harmonic Radiation (PLHR) consists of electromagnetic waves radiated by electric power systems at harmonic frequencies of 50 Hz or 60 Hz. On frequency-time spectrograms, they usually look like a set of intense parallel lines with mutual distances of 50/100 Hz or 60/120 Hz because odd/even harmonics can be strongly suppressed in some cases [8,13,14]. The hook electromagnetic radiation phenomenon is clearly recorded in Figure 2. From the figure, an obvious PLHR baseline can be seen near 2250 Hz (the baseline disappears after ut04:46), and electromagnetic radiation appears above the baseline. The latitude range is 46~53° s, and the L shell value is 3.3~4.4. Such electromagnetic radiation occurs more frequently during geomagnetic substorms, which may be associated with a large number of charged particles appearing in the magnetosphere. In this case, PLHR electromagnetic radiation is enhanced or weakened due to wave-particle interactions caused by a large number of energy particles encountered in the magnetic equatorial region [14]. In addition, PLHR can trigger chorus waves. When chorus waves of multiple frequency bands appear, the chorus excited by PLHR is easily confused with the chorus of magnetospheric whistlers, making it difficult to distinguish [15].

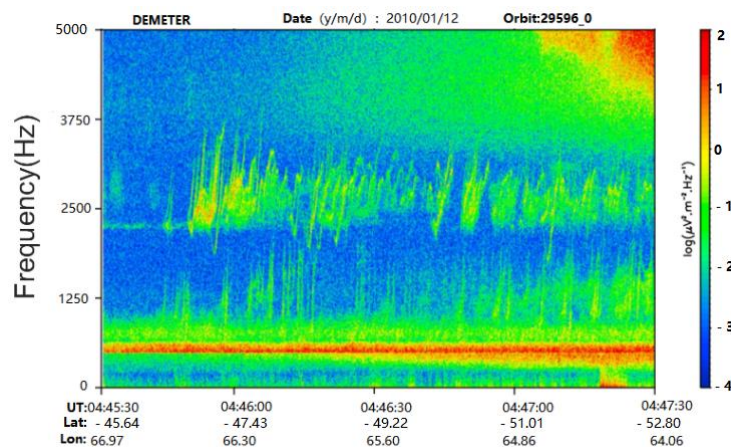


Figure 2. The spectrogram of VLF/ELF radiation signal excited by PLHR recorded by Demeter satellite on 12 January 2010.

The Zhangheng-1 (ZH-1) electromagnetic satellite was successfully launched at the Jiuquan Satellite Launch Center on 2 February 2018. It is China's first geophysical field exploration satellite. On the basis of absorbing the observation experience of the DEMETER satellite, it added loads, such as a high-precision magnetometer, GNSS occultation receiver, tri-frequency beacon, etc., and realized the comprehensive observation of ionospheric electromagnetic wave field in situ and structural parameters, and frequency bands and indicators in electromagnetic wave observation. ZH-1's main scientific goals are to obtain global electromagnetic field, plasma, high-energy particle observation and other data, and to provide scientific data services for short imminent earthquake prediction and geospatial physics research [16–19]. ZH-1 carried eight kinds of scientific loads [20] including an induction magnetometer, high-precision magnetometer [21], electric field detector (EFD), GNSS occultation receiver [22], plasma analyzer [23,24], high-energy particle detector [25], Langmuir probe [26] and Tri-band beacon transmitter etc. [27–30]. So far, ZH-1 has been in orbit for more than three years, collecting a large amount of global electromagnetic field waveform and power spectrum data. The space electric field detection is completed by the electric field detector (EFD), which provides basic data for the study of solar-terrestrial space physics, space weather, the interaction and effect between the ionosphere and upper atmosphere, magnetosphere, and provides data application services for seismic observation research [31]. The detection frequency band is divided into ULF (0~16 Hz), ELF(6 Hz~2.2 kHz), VLF(1.8 kHz~35 MHz), and the sampling rate of VLF is 50 kHz. ZH-1 generates about 10G of data every day. How to automatically identify electromagnetic wave anomalies from such huge observation data is particularly critical and urgent.

At present, there are relatively few studies on space electromagnetic wave disturbances on satellite spectrograms. Space electromagnetic wave disturbance automatic detection on the satellite spectrogram is in its infancy. The research mainly focuses on the automatic detection of L-shaped lightning whistlers [32] and horizontal electromagnetic waves [33,34]; no other automatic monitoring of space electromagnetic disturbances has been carried out. The main reasons are as follows: First, the electromagnetic spectrum data processing methods are backward, which makes the data lie in the hard disk column for a long time, enter the file or be deleted, the data are not fully utilized, and the value of the data cannot be reflected [35]. Second, some space electromagnetic wave disturbances have no significant characteristic definition on the spectrogram. Third, it is not clear how the morphological characteristics of different electromagnetic waves change after coupling in the ionosphere. It is a very challenging task to obtain space electromagnetic wave disturbance from a large amount of electromagnetic observation data manually.

So, this paper uses computer vision technology to automatically identify and locate other electromagnetic disturbances from massive electromagnetic data based on the phenomenon that the horizontal electromagnetic wave clarity reduces or disappears when it is disturbed by other spatial disturbances on the frequency-time spectrogram. Combined with space events and multi-dimensional information about time, space and orbit, it lays a certain foundation for further mining the global space-time transformation law of space events.

2. Materials and Methods

2.1. Data Collection

The data selected in this paper are the ZH-1 electric field VLF frequency band waveform data. According to the ZH-1 data specification, the electric field waveform data structure is shown in Table 1.

Table 1. Description of electric field VLF band data format instrument.

Name	Content	Type	Size	Unit
A133_W	Z	64-bit floating	$N \times 2048$	mV/m

A frequency-time spectrogram is obtained by using a short-time Fourier transform with the above-mentioned waveform data. Figure 3 is a frequency-time spectrogram, in which the ordinate represents the frequency, the abscissa represents the UT time, longitude and latitude of the satellite orbit, and the color bar on the right represents the electromagnetic wave intensity.

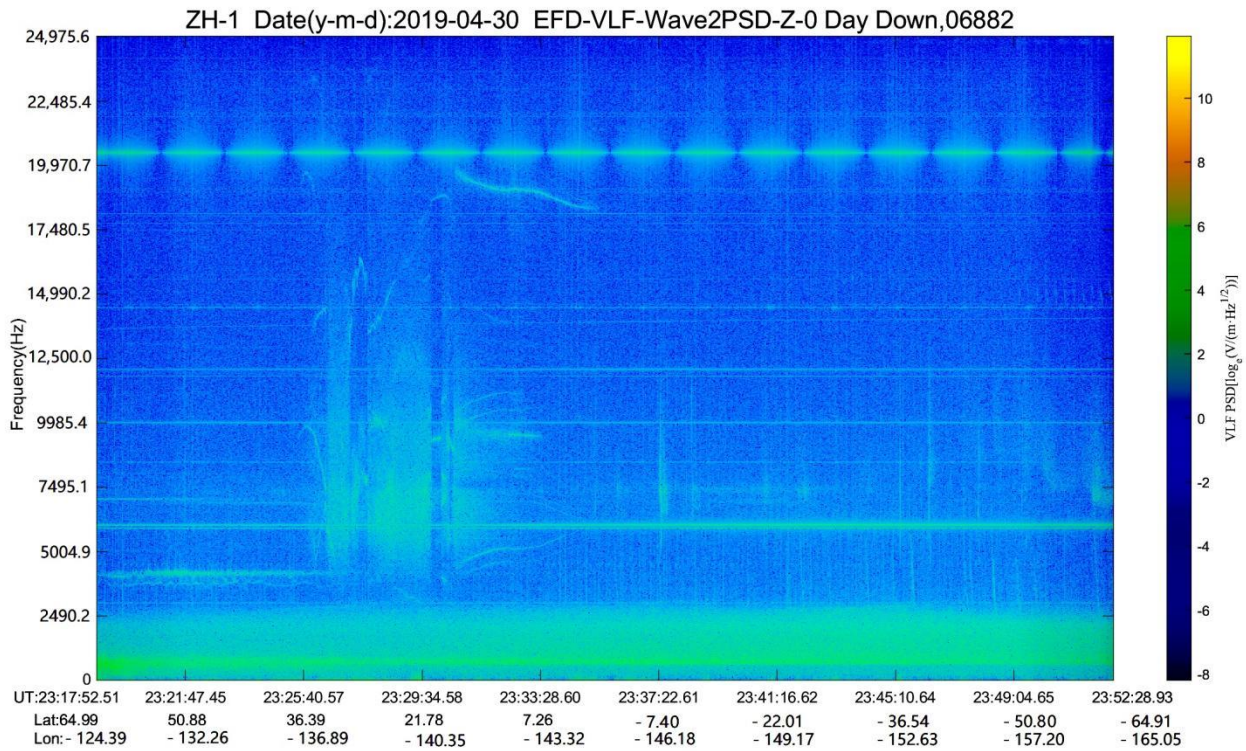


Figure 3. The VLF from 23:17 to 23:52 on 30 April 2019 spectrogram of ZH-1 EFD.

The electromagnetic wave interference automatic identification algorithm goal is to identify other space electromagnetic wave interference that affects the horizontal electromagnetic wave shape on a spectrogram. Therefore, the algorithm first needs to identify the horizontal line from the spectrogram, and then count the points of sparse morphological changes on the line to identify other electromagnetic wave interference. The algorithm flowchart is shown in Figure 4.

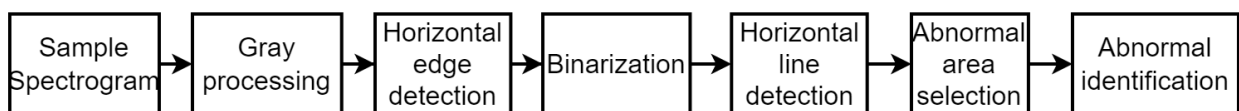


Figure 4. Automatic identification algorithm process.

2.2. Gray Processing

Observing the spectrogram, you will find that the horizontal electromagnetic waves identification is based on a straight line whose intensity is higher than the background on the spectrogram. No color feature is required, and gray processing is first used to eliminate the color influence, as shown in Figure 3. There are usually three gray processing methods [36].

Component method: take one of the three components of the spectrogram R, G, and B as the gray image value. Gray = RGB.B or Gray = RGB.G or Gray = RGB.R.

Maximum value method: Take the maximum value of the spectrogram R, G, B three-component brightness as the gray image value.

Weighted average method: The spectrogram R, G, and B components are weighted and averaged. Because the human eye is most sensitive to green and the least sensitive to blue, the grayscale formula is used as shown in Equation (1):

$$\text{Gray} = 0.114\text{RGB.B} + 0.587\text{RGB.G} + 0.299\text{RGB.R} \tag{1}$$

RGB represents the original spectrogram, RGB.R is the red channel value, RGB.G is the green channel value, and RGB.B is the blue channel value. Gray is the gray spectrogram.

According to the spectrogram color characteristics, the gray image obtained by taking the red channel has the best effect in the later recognition operation [35].

2.3. Horizontal Edge Feature Extraction

Traditional line detection uses Canny operator and Hough line transform for detection, which can detect lines at any angle. Canny operator is used to detect line edges in any direction, while the detection accuracy and detection rate of the Hough line transform algorithm are limited by the accumulator angle resolution, so the detection efficiency is low.

On the spectrogram, the horizontal electromagnetic wave disturbance mainly presents a horizontal shape higher than the background color, and a horizontal convolution kernel is used to extract the horizontal edge features [34]. The horizontal convolution kernel is shown in Equation (2).

$$\text{kernel} = [1, 0, -1] \tag{2}$$

The convolution kernel Equation (2) is brought into Equation (3) to realize the horizontal edge feature extraction.

$$\text{dst}(x, y) = \sum_{\substack{0 < x' < \text{kernel.cols}, \\ 0 \leq y' < \text{kernel.rows}}} \text{Kernel}(x', y') * \text{src}(x + x' - \text{anchor.x}, y + y' - \text{anchor.y}) \tag{3}$$

src is the original image; *dst* is the target image with the same size and channels number as the original image; *Kernel* is the convolution kernel which is a single channel floating-point matrix; *Anchor* is the anchor point of the kernel pointing to the relative position of the kernel filter point; *x, y* is the pixel coordinates on the original image, and *x', y'* is the convolution kernel pixel coordinates. Edge processing is calculated by the edge completion matrix in the convolution operation.

2.4. Binarization

Binarization is to set the pixel gray value to 0 or 255, which will make the image appear black and white. In order to separate the target from the background more quickly and accurately, the above operation result is processed by black and white binarization, and the calculation method is shown in Equation (4).

$$\text{dstmap}(x, y) = \begin{cases} \text{maxVal} & \text{if } \text{srcmap}(x, y) > \text{thresh} \\ 0 & \text{otherwise} \end{cases} \tag{4}$$

where *srcmap* represents the source image, *thresh* represents the threshold; *maxVal* represents the maximum value; *dstmap* represents the output image, and *x, y* represent the pixel coordinates.

2.5. Horizontal Line Detection Based on Unsupervised Learning

The clustering algorithm of machine learning is used to perform cluster analysis on the above result images to realize horizontal line detection. The selected clustering algorithm is the widely used Kmeans algorithm. The clustering analysis input data set is the white point coordinate set $P = \{px, py\}$ on the target image, where *px* and *py* are each point position in the image after binarization. Because only the horizontal electromagnetic wave in the

target image needs to be identified, the cluster number K is set to 2, and the two clusters are points on the straight line and points outside the straight line, respectively.

The Kmeans algorithm is as follows:

Step 1: Randomly select 2 sample data from the sample data to be clustered as the initial cluster center $\{\mu_1, \mu_2\}$.

Step 2: calculate the Euclidean distance from each sample to each initial cluster center, then select the nearest cluster center to form two clusters and update the two clusters according to the distance formula. The distance calculation is shown in Equation (5).

$$d = \sum_{i=1}^2 \sum_{p \in C_i} \|p - \mu_i\|_2^2 \quad (5)$$

μ_i is the cluster C_i central sample and p is the sample point.

Step 3: Recalculate cluster centers for the newly obtained two clusters. The cluster center calculation is shown in Equation (6).

$$\mu_i = \frac{1}{C_i} \sum_{p \in C_i} p \quad (6)$$

Repeat steps 2 and 3 until the termination condition $|\mu_{n+1} - \mu_n| \leq \varepsilon$ is satisfied or the preset number of iterations is reached, then the algorithm terminates.

After the above operation, not only the horizontal electromagnetic wave frequency value can be obtained, but also the retained pixel coordinate information on the straight line can be returned.

2.6. Selection of Abnormal Window on Horizontal Line

By observing the above marking results, it can be seen that in the space-time area disturbed by other electromagnetic waves, the horizontal electromagnetic wave clarity is reduced or even disappears, and the marking state is sparse or disappeared accordingly. The idea of the algorithm is: set a sliding window with width Dis and step size 1, scan each detected line from front to back, count the pixels' number on the unit length Dis as $PNum$, and calculate the window density d of each sliding window, as shown in Equation (7), where i represents the i -th sliding window.

$$d_i = \frac{PNum_i}{Dis} \quad (7)$$

If d_i is less than the density threshold th , that is, $d_i \leq th$, record d_i as an abnormal value.

Through a large number of experimental statistics, the sliding window density set $\{d_1, d_2, \dots, d_n\}$ on a straight line is basically not normally distributed. Figure 5 are statistical histograms of each sliding window density on the six horizontal lines from top to bottom marked by white arrows in Figure 6. Figure 6a is a spectrogram, and in order to facilitate observation, pixels on the straight line are marked in the form of red dots, as shown in Figure 6b, which are all skewed distributions. Therefore, the th value is selected through the box diagram. Figure 7 is the statistical box diagram of each sliding window density set on these six horizontal lines. $th = Q1 - (Q3 - Q1)$, where $Q1$ is the 25% quantile and $Q3$ is the 75% quantile.

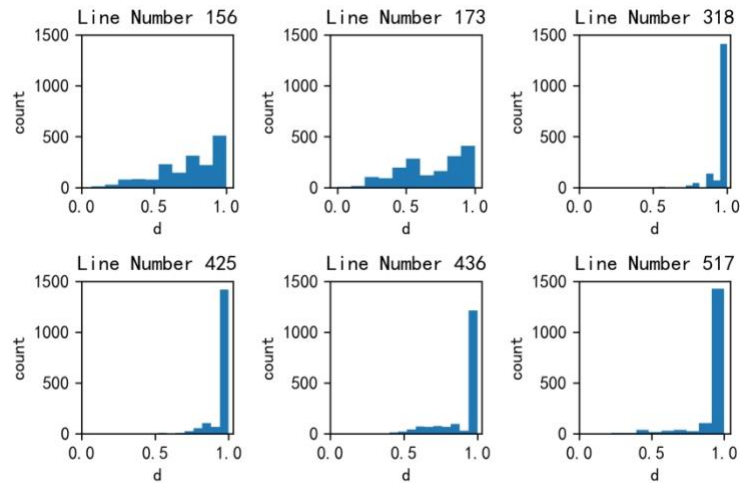


Figure 5. Histograms of the density of all windows on lines. Each subgraph represents a straight line, the title of each subgraph is the line number, and the histogram on each subgraph is the statistical distribution of the density of all the sliding Windows on a straight line. The density values range from 0 to 1, and the width of each column is 0.1. The abscissa represents the density value, and the ordinate represents the cumulative statistics that fall in a certain density range.

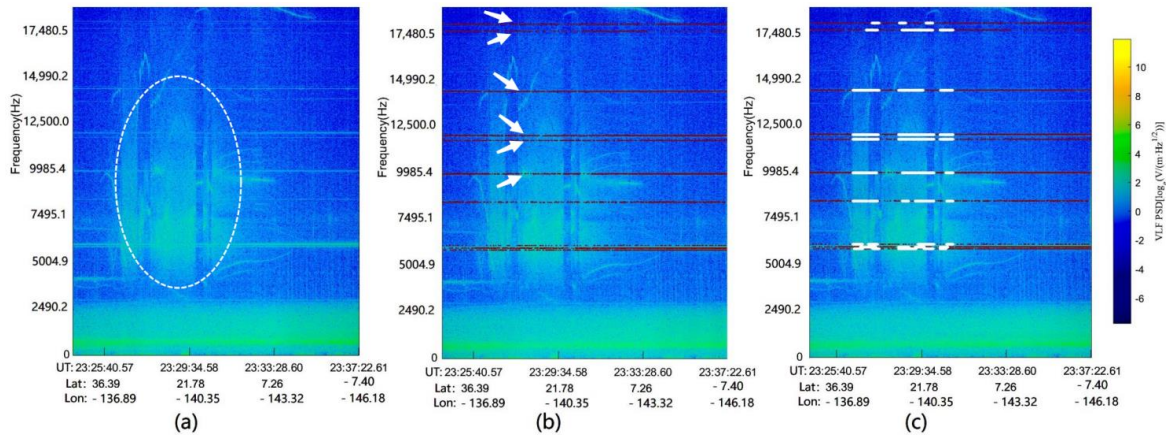


Figure 6. Display of test results. (a) Spectrogram generated by the Z-component waveform data of ZH-1 electric field VLF on 30 April 2019; (b) Detection results of horizontal lines marked by red dots; (c) Abnormal results marked by white lines.

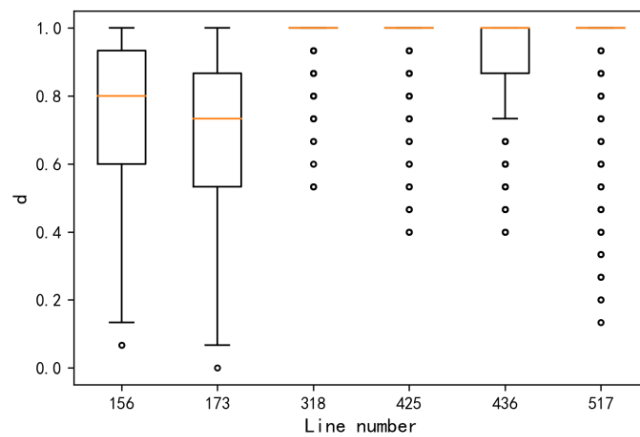


Figure 7. Box plots of the density of all windows on lines, and one box represents the density statistics of all sliding Windows on a line.

2.7. Abnormal Disturbance Identification

On the spectrogram, the horizontal line clarity is reduced, interrupted, or disappeared, which may be due to the other space electromagnetic waves interference or because the artificial emission source interrupts the emission or even the signal emitted by the artificial emission source itself is discontinuous, etc. Therefore, in some cases, the change of one horizontal line cannot be completely judged as to whether it is caused by other electromagnetic interference. Usually, n lines may exist and be detected on a spectrogram. If at the same time, more than m sliding windows on adjacent straight lines are marked as abnormal, the time is considered abnormal, and the time value and latitude and longitude value are recorded. In order to facilitate observation, a white line is used to mark anomalies on the horizontal line. The white line in Figure 6c is the result of detecting and marking anomalies on the line.

3. Results

3.1. Experimental Method

The experiment analyzed 500 spectrograms in 2019. There is horizontal electromagnetic wave interference and other electromagnetic wave interference on the spectrogram. This experiment uses Python 3.7 (Guido van Rossum, Amsterdam, Netherlands, www.python.org, accessed on 25 April 2022) programming language and calls the CV2 image library to implement the above detection process.

3.2. Experimental Results and Analysis

On the spectrogram, the area where the intensity can be observed by the human eye is significantly higher than the background is regarded as an abnormal area, as shown by the ellipse mark in Figure 6a. The experimental limits on the size of the abnormal area are as follows.

A sliding window is used to slide on each detected line, the size of the sliding window is set to Dis , and each sliding window density d_i determines whether an abnormality occurs. The sliding window Dis not only determines the disturbance interval in space and time but also affects the algorithm detection effect.

The abnormal disturbance detection algorithm is based on horizontal line clarity reduction, interruption, or disappearance, so it is first required to have horizontal electromagnetic wave interference on the spectrogram. If no horizontal line is detected on a spectrogram, the algorithm will not work. Moreover, the more horizontal lines on the spectrogram, the better the detection effect will be. Therefore, the spectrogram detected in this paper requires at least three horizontal lines to be detected. If it is less than three, it will not be brought into the detection algorithm. If there are n electromagnetic waves in the spectrogram, m of which are abnormal, a large number of experimental results show that the detection effect is the best when $\frac{m}{n} \geq \frac{3}{5}$ is satisfied, that is, if five straight lines are detected, and at least three straight lines are abnormal and are adjacent to each other. Adjacent refers to that at the same time, there cannot be more than two non-abnormal straight lines between the two straight lines where the abnormal window is located, otherwise, its abnormal mark will be canceled. Figure 8 is the result of abnormal detection and marking of multiple spectrograms when $Dis = 15$.

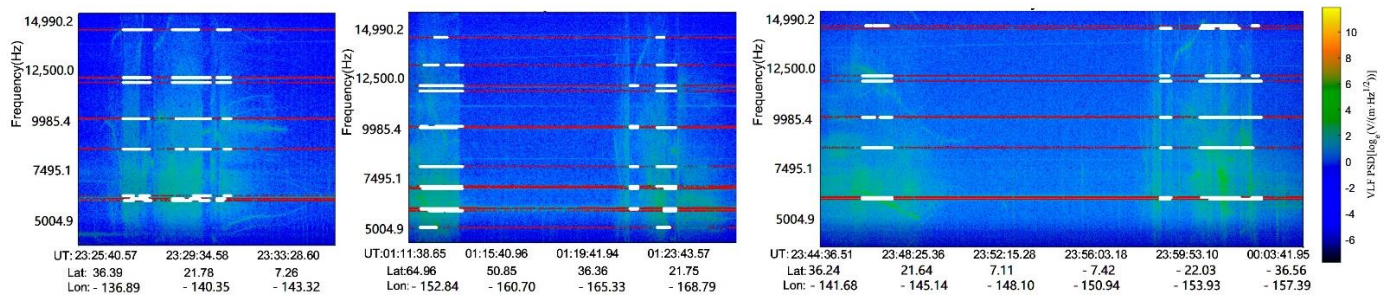


Figure 8. The automatic detection results of multiple abnormal disturbances are marked with white straight lines, $Dis = 15$.

Aiming at space electromagnetic wave disturbances with a wide frequency and time interval, the statistical analysis results of the detection experiments are shown in Figure 9. It can be seen from Figure 9 that the detection performance is poor when the window Dis is too large or too small. When the value is in the range $8 \leq Dis \leq 25$, the average detection effect is good.

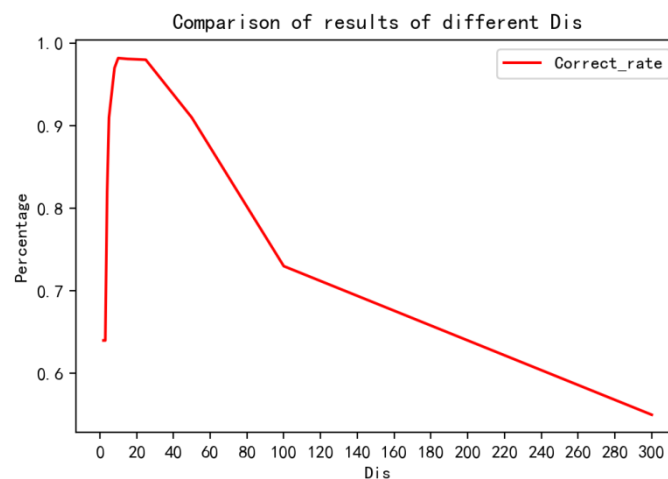


Figure 9. Comparison of detection statistics with different Dis values.

When $Dis = 15$, the correct rate is the highest, and the correct rate is 98.2%. The detection results are shown in Table 2. So, the frequency interval of the anomaly detected in this paper is defined as the disturbance area is $length \geq 15$ in the horizontal direction, and the disturbance area must traverse through more than three adjacent horizontal lines.

Table 2. Experimental result.

Dis	Correct Rate	Error Rate	Missed Rate
$Dis = 15$	0.982 ± 0.01	0.018 ± 0.003	0.005 ± 0.001

4. Discussion

The algorithm proposed in this paper detects the disturbance of space electromagnetic waves, but there are still many limitations, mainly as follows.

First, the detection algorithm has a certain pertinence, which is reflected in the requirements for the spectrogram. Because the detection is based on the horizontal lines' morphological changes, there must be more than three lines in the detected spectrogram. Second, the spectrogram shown in Figure 10a has a better detection effect on electromagnetic disturbances with a large and continuous time-frequency interval. The detection

and labeling result in the case of $Dis = 15$ is shown in Figure 10b. However, if the spectrograms are all vertical pulses, whistlers, etc., the electromagnetic disturbance detection effect shown in Figure 10d is very poor, as shown in Figure 10e. This is because the horizontal electromagnetic waves in each time interval on the spectrogram are disturbed, which not only affects the detection effect of the straight line, but also affects the density of all sliding windows on the straight line, and no outliers can be found.

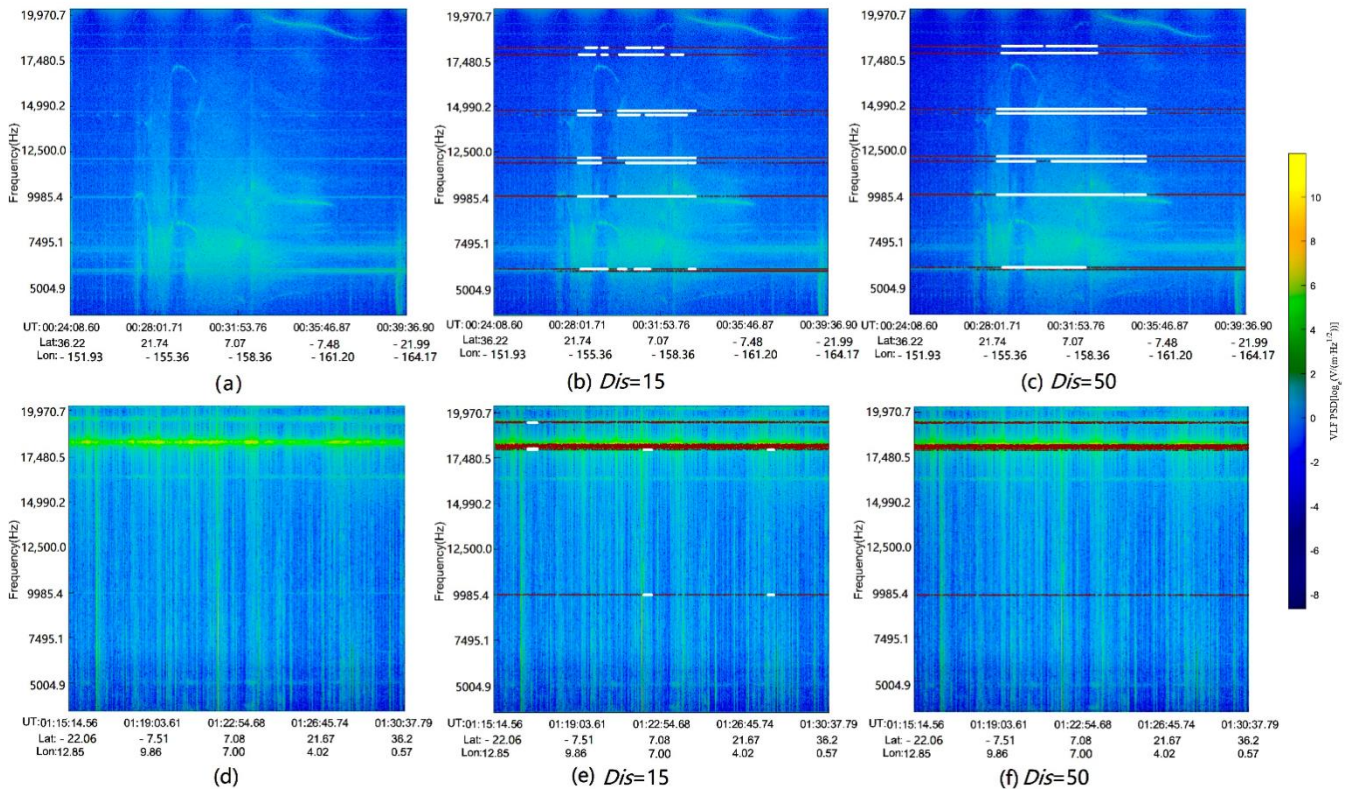


Figure 10. Comparison of spectrograms detection effects of different features.

In view of the above situation, and to improve the detection effect of the algorithm, one method is to use other existing detection methods for spectrograms, such as whistlers automatic detection [32], and explore new detection methods, and then combine various methods to detect. The second is to limit the detection targets for different needs. For example, the detection target is limited to the wide and continuous electromagnetic interference in the time interval, and targeted detection can be achieved by increasing the Dis value. When $Dis = 50$, the detection effect is still good for the wide and continuous electromagnetic interference in the time interval, as shown in Figure 10c, and some high-frequency pulses of electromagnetic interference can be filtered out, as shown in Figure 10f.

5. Conclusions

Because the electromagnetic wave in a horizontal shape on the spectrogram is disturbed by other space electromagnetic wave anomalies, which leads to the horizontal spectrum line weakening and interruption, this paper proposes an algorithm for the automatic detection of abnormal interference on the spectrogram of electric field VLF waveform data on ZH-1. According to the characteristics of spectral data, using computer vision technology, the automatic detection of abnormal spatial disturbance is realized through grayscale, horizontal feature enhancement, binarization processing, horizontal spectral line recognition and abnormal detection. The accuracy of the algorithm for detecting continuous electromagnetic wave disturbances with a wide frequency and time interval is up to 98.2%. It is helpful to further excavate abnormal disturbance events in space and study

short impending earthquake predictions. However, the algorithm has some limitations at present, and the focus of subsequent research will be to improve the algorithm on the basis of existing research so that all spatial abnormal disturbance events can have a good detection effect.

Author Contributions: Conceptualization and methodology, Y.H.; algorithm implementation, J.Y.; data analysis and conclusion, J.H.; software and investigation, Z.L.; writing—review and editing, X.S. All authors have read and agreed to the published version of the manuscript.

Funding: This research was funded by the Fundamental Research Funds for the Central Universities ZY20215143; National Key R&D program (2018YFC1503501); APSC Earthquake Project: Phase II; ISSI-BJ2019.

Institutional Review Board Statement: Not applicable.

Informed Consent Statement: Not applicable.

Data Availability Statement: Publicly available datasets were analyzed in this study. The CSES satellite electric field data can be found here: (www.leos.ac.cn, accessed on 1 September 2020).

Acknowledgments: This work made use of the data from the CSES mission, a project funded by China National Space Administration (CNSA) and the China Earthquake Administration (CEA). Thanks to the CSES satellite team for the data (www.leos.ac.cn, accessed on 1 September 2020).

Conflicts of Interest: The authors declare no conflict of interest.

References

1. Parrot, M.; Berthelier, J.J.; Lebreton, J.P.; Sauvaud, J.A.; Santolik, O.; Blecki, J. Examples of unusual ionospheric observations made by the DEMETER satellite over seismic regions. *Phys. Chem. Earth Parts* **2006**, *31*, 486–495. [[CrossRef](#)]
2. Larkina, V.I.; Nalivaiko, A.V.; Gershenzon, N.I.; Gokhberg, M.B.; Liperovskii, V.A.; Shalimov, S.L. Intercosmos-19 observation of VLF emissions associated with seismic activity. *Geomagn. Aeron.* **1983**, *23*, 842–846.
3. Chmyrev, V.; Isaev, N.; Bilichenko, S.; Stanev, G. Observation by space-borne detectors of electric fields and hydromagnetic waves in the ionosphere over an earthquake centre. *Phys. Earth Planet. Inter.* **1989**, *57*, 110–114. [[CrossRef](#)]
4. Parrot, M.; Mogilevsky, M. VLF emissions associated with earthquakes and observed in the ionosphere and the magnetosphere. *Phys. Earth Planet. Inter.* **1989**, *57*, 86–99. [[CrossRef](#)]
5. Pulinets, S.A.; Legen'Ka, A.D. Spatial–Temporal Characteristics of Large Scale Disturbances of Electron Density Observed in the Ionospheric F-Region before Strong Earthquakes. *Cosm. Res.* **2003**, *41*, 221–230. [[CrossRef](#)]
6. Liu, Y.M.; Wang, J.S.; Xiao, Z.; Suo, Y. A Possible Mechanism of Typhoon Effects on the Ionospheric F2 Layer. *Chin. J. Space Sci.* **2006**, *26*, 92–97.
7. Juntao, C.; Guo, Z.Z.; Yan, Z.; Tang, J.; Chen, X.B. The study on ionospheric disturbances during earthquakes. *Prog. Geophys.* **2007**, *22*, 695–701.
8. Parrot, M. DEMETER Observations of manmade waves that propagate in the ionosphere. *Comptes Rendus Phys.* **2018**, *19*, 26–35. [[CrossRef](#)]
9. Ryu, K.; Lee, E.; Chae, J.S.; Parrot, M.; Pulinets, S. Seismo-ionospheric coupling appearing as equatorial electron density enhancements observed via DEMETER electron density measurements. *J. Geophys. Res. Space Phys.* **2014**, *119*, 8524–8542. [[CrossRef](#)]
10. Zhang, X.; Zeren, Z.M.; Shen, X.H.; Jun, C.; Zhao, S.; Xiong, P.; Chen, H.; Ouyang, X. Analysis on variation of electric field spectrum at cut-off frequency before strong earthquakes: Taking 2006 Tonga M_W8.0 earthquake as an example. *Acta Seismol. Sin.* **2011**, *33*, 451–460.
11. He, Y.F.; Yang, D.M.; Chen, H.R. Demeter satellite detected the signal-to-noise ratio change of ground VLF transmitting station signal that may be related to Wenchuan earthquake. *Chin. Sci. Part D* **2009**, *39*, 403–4122009.
12. Zhang, X.M.; Shen, X.H.; Ouyang, X.Y.; Cai, J.A.; Huang, J.P.; Liu, J.; Zhao, S.F. Ionosphere VLF electric field anomalies before Wenchuan M 8 earthquake. *Dianbo Kexue Xuebao Chin. J. Radio Sci.* **2009**, *24*, 1024–1032.
13. Zeren, Z.M. Electromagnetic Waves Induced by Strong Earthquake and Non-Earthquake Sources in Geospace. Ph.D. Thesis, Beijing University of Aeronautics and Astronautics, Beijing, China, 2014.
14. Zhang, X.M.; Qian, J.D.; Ying, Y.; Zhao, S.-F.; Lou, W.-Y. Space Electromagnetic Disturbances Induced by High-voltage Power Lines. *Earthquake* **2019**, *39*, 11.
15. Parrot, M.; Manninen, J.; Santolík, O.; Němec, F.; Turunen, T.; Raita, T.; Macúšová, E. Simultaneous observation on board a satellite and on the ground of large-scale magnetospheric line radiation. *Geophys. Res. Lett.* **2007**, *34*, L19102. [[CrossRef](#)]
16. Shen, X.H.; Zong, Q.G.; Zhang, X.M. Introduction to special section on the China Seismo-Electromagnetic Satellite and initial results. *Earth Planet. Phys.* **2018**, *2*, 3–7. [[CrossRef](#)]

17. Li, Z.; Li, J.; Huang, J.; Yin, H.; Jia, J. Research on Pre-Seismic Feature Recognition of Spatial Electric Field Data Recorded by CSES. *Atmosphere* **2022**, *13*, 179. [[CrossRef](#)]
18. Cao, J.B.; Yang, J.Y.; Lu, L. Non-seismic Induced Electromagnetic Waves in the Near Earth Space. *Earthquakes* **2008**, *29*, 17–25. (In Chinese)
19. Wang, Z.; Zhou, C.; Zhao, S.; Xu, X.; Liu, M.; Liu, Y.; Liao, L.; Shen, X. Numerical Study of Global ELF Electromagnetic Wave Propagation with Respect to Lithosphere–Atmosphere–Ionosphere Coupling. *Remote Sens.* **2021**, *13*, 4107. [[CrossRef](#)]
20. Wang, L.; Hu, Z.; Shen, X. Data processing methods and procedures of CSES satellite. *J. Remote Sens.* **2018**, *22*, 39–55.
21. Zhou, B.; Cheng, B. Development and calibration of high-precision magnetometer of the China Seismo-Electromagnetic satellite. *Natl. Remote Sens. Bull.* **2018**, *22*, 64–73.
22. Diego, P.; Huang, J.; Piersanti, M.; Badoni, D.; Zeren, Z.; Yan, R.; Rebutini, G.; Ammendola, A.; Candidi, M.; Guan, Y.-B.; et al. The Electric Field Detector on Board the China Seismo Electromagnetic Satellite-In-Orbit Results and Validation. *Instruments* **2020**, *5*, 1. [[CrossRef](#)]
23. Lu, H.X.; Shen, X.H.; Zhao, S.F.; Liao, L.; Lin, J.; Huang, J.; Zeren, Z.; Sun, F.; Guo, F. Typical event observation of the tri-band beacon onboard the CSES (ZH-1) satellite. *Chin. J. Radio Sci.* **2022**, *36*, 1–8.
24. Liu, C.; Guan, Y.; Zheng, X.; Zhang, A.; Piero, D.; Sun, Y. The technology of space plasma in-situ measurement on the China Seismo-Electromagnetic Satellite. *Sci. China Technol. Sci.* **2018**, *62*, 829–838. [[CrossRef](#)]
25. Yan, R.; Shen, X.H.; Huang, J.X.; Wang, Q.; Chu, W.; Liu, D.; Xu, S. Examples of unusual ionospheric observations by the CSES prior to earthquakes. *Earth Planet. Phys.* **2018**, *2*, 515–526. [[CrossRef](#)]
26. Rui, Y.; Zhe, H.; Wang, L.; Guan, Y.; Liu, C. Preliminary data inversion method of Langmuir probe onboard CSES. *Acta Seismol. Sin.* **2017**, *39*, 239–247.
27. Zhou, B.; Yang, Y.; Zhang, Y.; Gou, X.; Cheng, B.; Wang, J.; Li, L. Magnetic field data processing methods of the China Seismo-Electromagnetic Satellite. *Earth Planet. Phys.* **2018**, *2*, 455–461.
28. Wang, L.; Shen, X.; Zhang, Y.; Zhang, X.; Hu, Z.; Yan, R.; Yuan, S.; Zhu, X. Developing progress of China Seismo-Electromagnetic Satellite project. *Acta Seismol. Sin.* **2016**, *38*, 376–385+509.
29. Wang, X.T.; Yang, D.H.; Zhou, Z.H.; Cui, J.; Zhou, N.; Shen, X. Features of topside ionospheric background over China and its adjacent areas obtained by the ZH-1 satellite. *Chin. J. Geophys.* **2021**, *64*, 391–409.
30. Shen, X.; Zhang, X.; Cui, J.; Zhou, X.; Jiang, W.L.; Gong, L.X.; Liu, Q.Q. Remote sensing application in earthquake science research and geophysical fields exploration satellite mission in China. *Natl. Remote Sens. Bull.* **2018**, *22*, 1–16.
31. Ma, M.; Lei, J.; Li, C. Design Optimization of Zhangheng-1 Space Electric Field Detector. *J. Vac. Sci. Technol.* **2018**, *38*, 582–589.
32. Yuan, J.; Wang, Q.; Yang, D.H. Automatic recognition algorithm of lightning whistlers observed by the Search Coil Magnetometer onboard the Zhangheng-1 Satellite. *Chin. J. Geophys.* **2021**, *64*, 3905–3924. [[CrossRef](#)]
33. Han, Y.; Yuan, J.; Feng, J.L.; Yang, D.; Huang, J.; Wang, Q.; Zeren, Z. Automatic detection of “horizontal” electromagnetic wave disturbance in the data of EFD on ZH-1. *Prog. Geophys.* **2021**, *36*, 2303–2311.
34. Han, Y.; Yuan, J.; Feng, J.L.; Yang, D.; Huang, J.; Wang, Q.; Zeren, Z. Automatic detection of horizontal electromagnetic wave disturbance in Zhangheng-1 EFD data based on horizontal convolution kernel. *Prog. Geophys.* **2022**, *37*, 11–18.
35. Wu, Q.H.; Ding, G.R.; Sun, J.C. *Electromagnetic Spectrum Data Mining Theories and Applications*; Science Press: Beijing, China, 2020.
36. Zhang, Y.J. *A Course of Image Processing and Analysis*, 2nd ed.; People Post Press: Beijing, China, 2016.